JPhys Energy

PAPER • OPEN ACCESS

Modification of TiO_2 with metal chalcogenide nanoclusters for hydrogen evolution

Journal of Physics: Energy

PAPER

Modification of TiO_2 with metal chalcogenide nanoclusters for hydrogen evolution

Stephen Rhatigan[1], Lorenzo Niemitz[1] and Michael Nolan[1,2]

[1] Tyndall National Institute, UCC, Lee Maltings, Dyke Parade, Cork T12 R5CP, Ireland
[2] NIBEC, Ulster University, Shore Road, Co Antrim BT37 OQB, United Kingdom

E-mail: Michael.nolan@tyndall.ie

Keywords: photocatalysis, TiO_2, sulphides, selenides, hydrogen evolution reaction, DFT + U

Supplementary material for this article is available online

OPEN ACCESS

RECEIVED
10 September 2020

REVISED
15 January 2021

ACCEPTED FOR PUBLICATION
8 February 2021

PUBLISHED
3 March 2021

Abstract

Using density functional theory, corrected for on-site Coulomb interactions (DFT + U), we have investigated surface modification of TiO_2 with metal chalcogenide nanoclusters for hydrogen evolution. The nanoclusters have composition M_4X_4 (M = Sn, Zn; X = S, Se) and are adsorbed at the rutile (110) surface. The nanoclusters adsorb exothermically, with adsorption energies in the range −2.8 eV to −2.5 eV. Computed density of states (DOS) plots show that cluster-derived states extend into the band-gap of the rutile support, which indicates that modification produces a redshift in light absorption. After modification, photoexcited electrons and holes are separated onto surface and cluster sites, respectively. The free energy of H adsorption is used to assess the performance of metal chalcogenide modified TiO_2 as a catalyst for the hydrogen evolution reaction (HER). Adsorption of H at nanocluster (S, Se) and surface (O) sites is considered, together with the effect of H coverage. Adsorption free energies at cluster sites in the range −0.15 eV to 0.15 eV are considered to be favourable for HER. The results of this analysis indicate that the sulphide modifiers are more active towards HER than the selenide modifiers and exhibit hydrogen adsorption free energies in the active range, for most coverages. Conversely, the adsorption free energies at the selenide nanoclusters are only in the active range at low H coverages. Our results indicate that surface modification with small, dispersed nanoclusters of appropriately selected materials can enhance the photocatalytic activity of TiO_2 for HER applications.

1. Introduction

Photocatalytic water splitting, wherein solar energy is converted to chemical energy, stored in the bonds of hydrogen gas (H_2), is a promising strategy for the production and storage of clean, renewable fuel. Solar driven water splitting proceeds at the surface of a semiconductor photocatalyst material as two half reactions, mediated by photoexcited electrons and holes. The half reactions are the oxygen evolution reaction (OER) and the hydrogen evolution reaction (HER), which are oxidation and reduction reactions, respectively. Each of these reactions requires catalyst architectures that are tailored for their promotion and technologies for overall water splitting will incorporate multifunctional components for optimal efficiency.

Among the most studied photocatalytic materials is titanium dioxide (TiO_2) [1–7]; TiO_2 is a cheap, non-toxic and abundant material, which is stable under photocatalytic operating conditions. However, the large band gap of TiO_2 (>3 eV) restricts its activity to the UV range of the solar spectrum. Thus, in order to maximise the ambient solar-driven photocatalytic capacity of titania-based materials, it is necessary to modify the electronic structure to induce a redshift in light absorption. Moreover, oxide-based photocatalysts are well studied for water oxidation [8, 9]; that is, the OER half reaction. They are unsuitable for the HER without a co-catalyst. This is because H ions bind too strongly to the oxygen ions of the catalyst surface to form surface bound hydroxyls.

Typically, co-catalysts are employed to promote the HER and the most efficient co-catalyst materials are the platinum-group metals (PGMs) [8]. PGMs are critical materials, which are rare and expensive; this limits their implementation, and thus, the viability of water splitting technologies. This provides the impetus for the considerable scientific effort devoted to the discovery of new, cheap and earth-abundant materials for efficient HER catalysis. In this endeavour, chalcogenides (sulphides, selenides and tellurides) have been demonstrated to catalyse the HER with efficiencies approaching those of the PGMs [8, 10]. In particular, layered transition metal dichalcogenides (TMDs), containing sulphur or selenium, have garnered interest due to high HER activities [11, 12]. Through combinations of experiment and first-principles simulations, low-coordinated chalcogen sites at the edges of these layered TMDs have been identified as the active sites for HER [13–15].

There are two proposed pathways for the two-step HER mechanism: the Volmer–Tafel reaction and the Volmer–Heyrovsky reaction [8, 16]. Here, we restrict ourselves to acidic media, as this is beneficial for the HER activity [17, 18]. The Volmer step is common to both pathways and may be described as:

$$\text{Volmer:} \qquad H^+ + e^- \rightarrow H_{ads}.$$

In the Volmeer step, an electron is transferred to a proton at an adsorption site of the catalyst surface, resulting in a surface bound H species (H_{ads}). The HER reaction is completed with desorption of a H_2 molecule, which can proceed via a Tafel or Heyrovsky process:

$$\text{Tafel:} \qquad H_{ads} + H_{ads} \rightarrow H_2.$$

$$\text{Heyrovsky:} \qquad H_{ads} + H^+ + e^- \rightarrow H_2.$$

For optimal HER activity, there must be a balance between the competing adsorption and desorption steps. A widely accepted computational descriptor for this balance is the Gibbs free energy of adsorption of a H atom (ΔG_H) at the catalyst surface [19]. This is termed the computational hydrogen electrode model and permits a rapid comparison and assessment of different catalysts and potential active sites for H adsorption.

DFT computations of the free energy of H adsorption at low-coordinated edge sites of MoS_2 revealed that this quantity, ΔG_H, was close to thermoneutral (0 eV) and was comparable to that computed for Pt [20]. Conversely, ΔG_H for sites in the MoS_2 basal plane were endothermic and so the basal plane is inactive for HER. Similar studies have been performed on a range of sulphides [15, 21–23], selenides [22, 23] and phosphides [24–26] and show that ΔG_H provides a useful descriptor for screening materials and sites for their HER activity. Values for ΔG_H that are close to 0 eV are desirable, in accordance with the Sabatier principle. If the interaction is too strongly exothermic, the H ions will bind too strongly to the surface and if H adsorption is too uphill, or endothermic, no reaction will take place [20, 24].

In this work, we examine modification of the TiO_2 rutile (110) surface with nanoclusters of composition M_4X_4 (M = Sn, Zn; X = S, Se). Surface modification in this way can be performed using atomic layer deposition (ALD) [27], incipient wetness impregnation [28–30], or chemisorption-calcination cycles [7, 31] and permits modulation of the light absorption properties of the titania substrate, promotes separation and stability of photoexcited electrons and holes, and provides low coordinated active sites for catalytic reactions. We have studied surface-modified TiO_2 for water oxidation [32] and CO_2 activation [33, 34]. In the context of hydrogen evolution, this strategy enables us to combine the desirable properties of TiO_2 through modification with nanoclusters that display low-coordinated, active chalcogen sites, which promote the HER.

By computing the projected electronic density of states (PEDOSs), we analyse the impact of modification on the energy gap and light absorption. The modification with the chalcogen nanoclusters extends the valence band maximum (VBM) to higher energies, thereby inducing a redshift in light absorption compared to unmodified TiO_2. We impose a triplet electronic state on the system to model photoexcitation and with this model, we compare the spatial separation and stability of photoexcited charges. Modification promotes the separation of electrons and holes and enhances their stability in the excited state.

Finally, we investigate the HER activity of the modified surface via computations of ΔG_H. To be consistent with the literature and allow for errors in computed energies within the DFT set-up, we consider the range of $\Delta G_H = (-0.15 \text{ eV to } +0.15 \text{ eV})$ to be relevant for assessment of the potential for HER. As metal oxide surfaces easily form surface bound hydroxyls [35], we first compute ΔG_H for H adsorbed at sites of the titania support and consider coverages that range from 1H to enough hydrogen to saturate the available surface sites. For H adsorption at surface sites, we consider only the bridging oxygen sites (O_{br}) that have no interfacial bonds with the nanocluster modifier. For each surface H coverage, we then compute ΔG_H for H adsorption at cluster sites. In these calculations, all chalcogen sites of the modifiers are considered and the most stable configurations that we find are discussed. We find that the sulphide modifiers exhibit free

energies close to thermoneutral and within our desired range at most coverages. By contrast, for the selenide modifiers, the cluster sites are active only for low surface coverages of H. We rationalise these findings on the basis of the electronic structure of the chalcogen modifiers and propose metal sulphide-modified TiO_2 as a material for hydrogen evolution.

2. Methodology

All calculations are performed in a periodic plane wave basis set with the VASP5.4 [36, 37] code. Calculations are spin polarised and use projector augmented wave potentials [38, 39] to describe the core–valence electron interactions. The Perdew–Wang (PW91) approximation to the exchange correlation functional is used [40]. This functional was used in our earlier studies of nanocluster modified TiO_2 [33, 41, 42] and thus provides a consistent description of nanocluster-modified TiO_2 models, which facilitates comparison across these materials. Moreover, our models based on the PW91 functional have corroborated experimental observations in collaborative studies of doped TiO_2 and modified TiO_2 surfaces [32, 43, 44].

The plane-wave energy cut-off is 400 eV; Ti is described with four valence electrons; Sn with 14; Zn with 12; O, S and Se with six; and H with one. The convergence criteria for the energy and forces are 10^{-4} eV and 0.02 eV $Å^{-2}$, respectively. The k-points are sampled using a $(4 \times 4 \times 1)$ grid and aspherical gradient corrections are applied throughout. Gaussian smearing with $\sigma = 0.1$ eV is implemented in calculations of the DOS. Additional, single-point calculations, using PBE0, which has 25% exact exchange [45, 46], were performed on the DFT + U relaxed geometries. For these calculations, a $(2 \times 2 \times 1)$ k-point sampling grid was used.

A Hubbard U correction is applied to the Ti and Zn 3d states with U(Ti) = 4.5 eV and U(Zn) = 7.8 eV, consistent with previous work [47–53]. These corrections are necessary in describing the partially filled d-orbital and reduced Ti^{3+} states [54, 55] and to address shortcomings in the standard GGA description of Zn electronic states [53]. An additional +U correction is applied to the O 2p, S 3p, and Se 4p states (U = 5.5 eV) in the photo-excited state model to describe hole localisation [32, 41, 42, 56]. We do not apply +U to anion 2p states for other calculations as this would make comparisons with computational studies in the literature difficult.

The bulk lattice parameters for rutile are computed as $a = b = 4.638$ Å and $c = 2.973$ Å. The model for the rutile TiO_2 substrate consists of a 12 atomic layer slab in a (2 ×4) expansion of the (110) surface. Periodic images are separated by a vacuum gap of 10 Å. Thus, the supercell dimensions are 13.120 Å × 11.896 Å × 20.680 Å. Four metal-chalcogenide nanocluster modifiers, of compositions Sn_4S_4, Sn_4Se_4, Zn_4S_4 and Zn_4Se_4 are first relaxed in the gas phase (see figure S1 in the supplementary material (available online at stacks.iop.org/JPENERGY/3/025001/mmedia) and then adsorbed in different configurations at the rutile (110) surface. The adsorption energies are computed using:

$$\Delta E_{ads} = E_{NC@r110} - E_{r110} - E_{NC} \quad (1)$$

Where $E_{NC@r110}$, E_{r110}, and E_{NC} are the energies of the composite surface, the bare surface, and the gas-phase NC, respectively. These energies can be thought of as describing the stability of the modifier on the TiO_2 substrate. Thus, a large ΔE_{ads} signifies that the modifier would only desorb at high temperatures. We adopt the notation M_4X_4-r110 (M = Sn, Zn; X = S, Se) for these composite surfaces.

Regarding the size of these nanoclusters, these models have been previously used [53] and our older work with Tada and co-workers [7, 57–59] showed that smaller nanoclusters deposited onto TiO_2 showed higher activity and therefore small, sub-nm nanoclusters are likely to be the most active, while their deposition can be well controlled through ALD techniques.

The systems under study in the current work consist of metal chalcogenide nanoclusters in intimate contact with the rutile surface. The nanocluster and surface interact via the formation of interfacial bonds and this establishes new energy levels. The impact of modification on the light absorption properties will depend on the positions of these levels relative to the VBM and CBM of the support. Calculations of the energy gaps and band alignments of the isolated materials have been the subject of a number of papers [60, 61], and this is useful in the rational selection of possible modifiers. However, due to the intimate nature of the interface, one cannot determine, *a priori*, the impact of surface modification based on these considerations. Thus, we compute the projected DOS for the M_4X_4-r110 and implement a model for photoexcitation, described below, to elucidate the light absorption properties of the composite surfaces.

Photoexcitation is modelled by imposing a triplet electronic state on the system. This forces an electron from the filled valence band to the empty conduction band, leaving a hole in the valence band. This computational approach has been used in previous work [32, 33, 41, 42] and is described in detail in the supplementary material. We use this model to assess the impact of modification on the optical band gap, the stability and spatial separation of charges in the excited state.

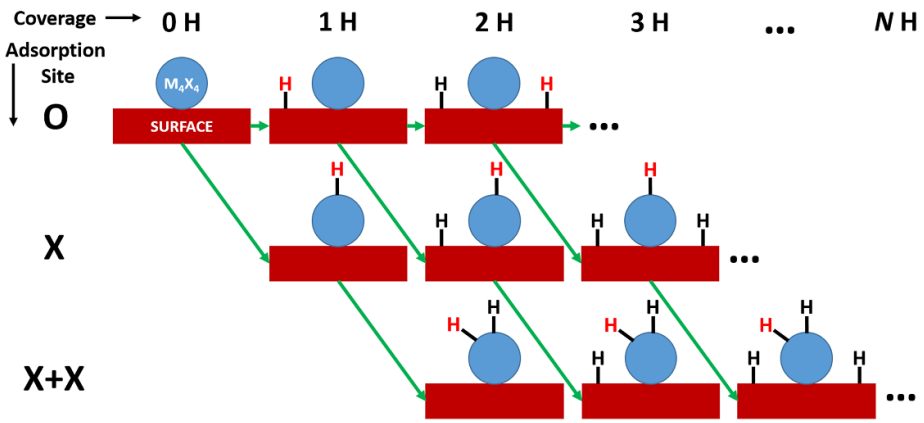

Figure 1. Schematic of the workflow for the study of hydrogen adsorption at the M_4X_4-modified rutile (110) surface. In the first set of calculations, shown in the top row, H atoms are adsorbed at the titania surface, up to saturation of the surface (O_{br}) sites. In the second set of calculations, shown in the second row, for each coverage of H at the TiO_2 surface, one H is adsorbed at a site on the chalcogenide nanocluster. For those configurations for which the hydrogen adsorption free energy at a cluster site is in the active range, we proceed with the third set of calculations in which a second H is adsorbed at a chalcogen nanocluster site, as shown in the third row. In each image, the red H represents the current calculation.

Hydrogen adsorption is examined at both the surface and the nanocluster. We explore adsorption of H at twofold coordinated bridging O ions (O_{br}) of the rutile (110) surface and at chalcogen sites of the modifiers. We follow the workflow shown in the schematic in figure 1 and begin with H adsorption at O_{br} surface sites. These calculations, represented by the top row of figure 1, are performed first and we identify the most stable configuration for each hydrogen coverage ranging from 0 H to saturation of the surface sites. The adsorption energy of the nth H atom at the most stable surface with an existing coverage of $(n-1)$H atoms is computed via:

$$\Delta E_{\mathrm{H}} = E_{n\mathrm{H@surf}} - E_{(n-1)\mathrm{H@surf}} - \frac{1}{2}\left(E_{\mathrm{H_2}}\right) \tag{2}$$

Where $E_{n\mathrm{H@surf}}$, $E_{(n-1)\mathrm{surf}}$, and $E_{\mathrm{H_2}}$ are the computed energies of the surface with nH atoms adsorbed, the surface with $(n-1)$H atoms, and an isolated, gas phase H_2 molecule.

In the second set of calculations, represented by the second row of figure 1, for each surface coverage of hydrogen, we examine hydrogen adsorption at chalcogen sites. For a surface coverage of $(n-1)$H, the adsorption energy of the n^{th} H atom at a cluster site is computed via:

$$\Delta E_{\mathrm{H}} = E_{\mathrm{H@cluster}} - E_{(n-1)\mathrm{H@surf}} - \frac{1}{2}\left(E_{\mathrm{H_2}}\right) \tag{3}$$

Where $E_{\mathrm{H@cluster}}$ is the energy of the system with 1H at a cluster site and $(n-1)$H adsorbed at surface sites. These calculations elucidate the impact of surface hydrogen coverage on the strength of interaction between H and the cluster site. For those configurations with adsorption free energies within our range, we proceed with the third set of calculations, represented by the third row in figure 1, and examine adsorption of a second H atom at a cluster site to assess any trends in H coverage on the nanocluster modifier.

From the chemisorption energies (ΔE_{H}), we compute the free energy of adsorption using:

$$\Delta G_{\mathrm{H}} = \Delta E_{\mathrm{H}} + \Delta E_{\mathrm{ZPE}} - T\Delta S_{\mathrm{H}} \tag{4}$$

Where ΔE_{ZPE} is the difference in zero point energy (ZPE) between the H atom adsorbed at the surface and in the gas phase; and $T\Delta S_{\mathrm{H}}$ accounts for the difference in entropy between the final and initial state. The zero point energies, for the gas phase H_2 molecule and for H adsorbed at O, S and Se sites, are derived from computations of the vibrational frequencies, according to the method prescribed in the work of Liao *et al* [62]. For adsorption, only the vibrations of the H ion and the surface/cluster site (O, S, Se) to which it is adsorbed are considered; the ZPE for the adsorption site is then subtracted from this value. As is typical in such studies, the entropic contributions for H adsorbed at the surface are omitted, and so the value for $-T\Delta S_{\mathrm{H}}$ is taken as half the value for molecular H_2. Thus, the ZPE and entropic contributions to the free energy are obtained from:

$$\Delta E_{\mathrm{ZPE}} - T\Delta S_{\mathrm{H}} = \left(\mathrm{ZPE}_{H^*} - \frac{1}{2}\mathrm{ZPE}_{\mathrm{H^2}}\right) - \left(0 - \frac{1}{2}T\Delta S_{\mathrm{H^2}}\right). \tag{5}$$

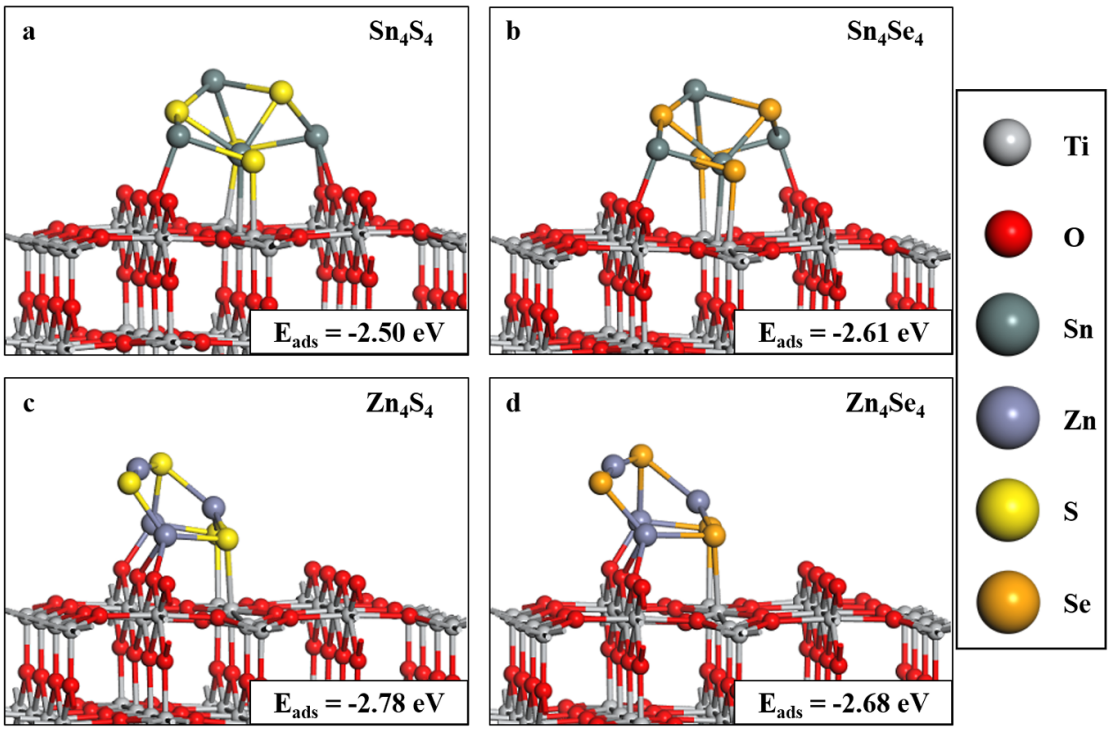

Figure 2. Relaxed geometries of (a) Sn_4S_4-, (b) Sn_4Se_4-, (c) Zn_sS_4-, and (d) Zn_4Se_4-r110. The adsorption energies of the nanoclusters at the rutile (110) surface are included in the insets. The colour scheme in the legend on the right applies to this and subsequent figures.

In this way, we compute $\Delta E_{ZPE} - T\Delta S_H$ values of 0.35, 0.29, and 0.26 eV for H adsorbed at O, S, and Se sites, respectively, which are consistent with other values used in the literature [24, 62–64].

3. Results

3.1. Atomic structure

The relaxed structures of the M_4X_4-r110 are shown in figure 2; the computed adsorption energies are included in the insets. The negative adsorption energies indicate that the modifier–surface interaction is favourable and the magnitudes of these energies suggest that the nanoclusters are strongly bound at the surface [32, 33, 41, 42, 56].

For Sn_4S_4-r110, shown in figure 2(a), there are two Ti–S bonds of length 2.5 Å and three Sn–O bonds of lengths 2.2–2.4 Å. For Sn_4Se_4-r110, in figure 2(b), there are two Ti–Se bonds of lengths 2.7 and 2.8 Å and two Sn–O bonds of length 2.2 Å. For both Sn_4S_4-r110 and Sn_4Se_4-r110, an additional bond forms between one Sn ion and a surface Ti with a bond length of 2.9 Å.

For Zn_4S_4-r110, shown in figure 2(c), there are two Ti–S bonds, both of length 2.5 Å and three Zn–O bonds; one Zn–O bond is 1.9 Å and two have length 2.1 Å. For Zn_4Se_4-r110, in figure 2(d), there are two Ti–Se bonds of lengths 2.6 and 2.7 Å and three Zn–O bonds of lengths 1.9, 2.1 and 2.1 Å.

From these data, we can see that the Ti–S bonds are shorter than the Ti–Se bonds. This is expected as Se has a larger ionic radius than S [8, 10]. Nanocluster metal–S bonds are also shorter than metal–Se bonds, both in the gas-phase and after adsorption at the rutile TiO_2 surface. Metal–S bonds are consistently shorter by 0.12–0.16 Å, than equivalent bonds in the selenide structures. These values are in agreement with the ionic radii of S^{2-} and Se^{2-}, which are 1.84 and 1.98 Å, respectively [65]. However, despite differences in the composition of the nanocluster modifiers, the adsorption energies are similar in all cases.

3.2. Density of states

The PEDOS plots, computed for the M_4X_4-r110 heterostructures, are shown in figure 3. The VBM of the titania support has been set to 0 eV and the band gap of the rutile (110) surface, from this computational set-up, is 2.20 eV. After modification, occupied cluster-derived electronic states, which are predominantly chalcogen *p* states, extend into the energy gap. Occupied states emerge at 1.18, 1.30, 1.33 and 1.57 eV above the titania VBM for modification with Sn_4S_4, Sn_4Se_4, Zn_4S_4 and Zn_4Se_4, respectively. This is combined with an enhancement of the DOS near the VBM of the titania support due to modification. Moreover, for Sn_4X_4

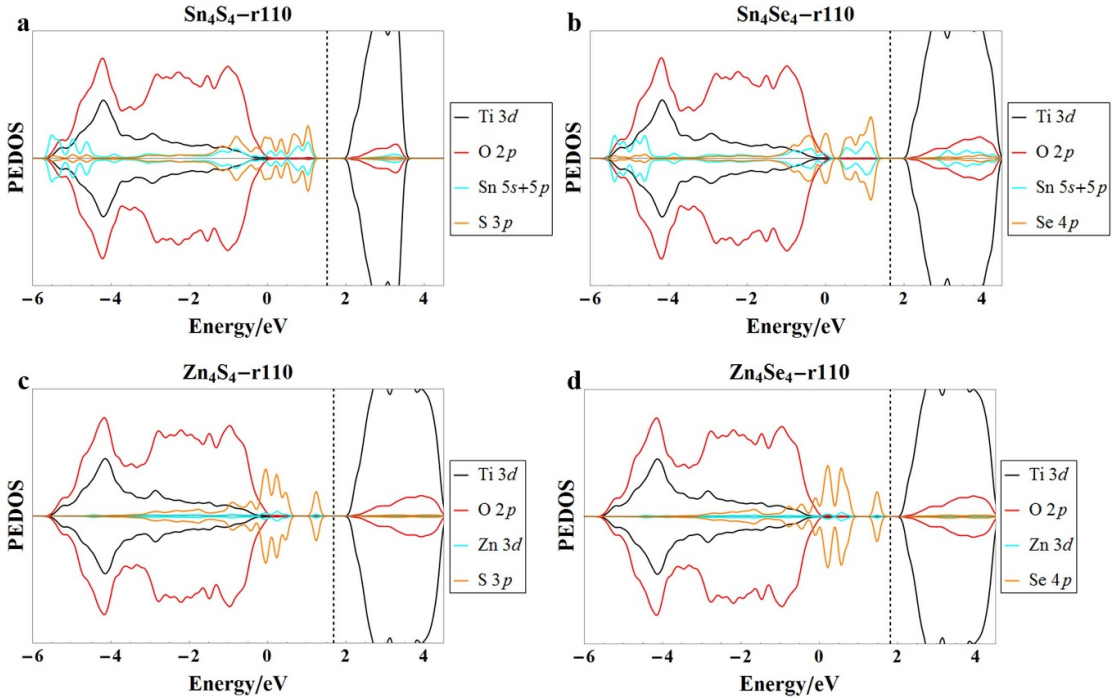

Figure 3. Density of states (DOS) plots for (a) Sn_4S_4-, (b) Sn_4Se_4-, (c) Zn_4S_4-, and (d) Zn_4Se_4-r110. The VBM of the titania support is set to 0 eV and the dashed vertical lines indicate the Fermi level. Nanocluster contributions, (M = Sn, Zn and X = S, Se), are shown (×10) for clarity.

modification, Sn-derived states emerge in the energy gap. These states are due to the lone pair, as has been discussed in previous work on Sn chalcogenides [66, 67].

To confirm these results, single-point PBE0 calculations, with 25% exact enchange, were performed on the DFT + U relaxed geometries. The resulting PEDOS plots are presented in figure S3 of the *supporting information* document. While there are quantitative differences in the description of the electronic structure and the extent to which cluster-derived states extend into the titania energy gap, both computational set-ups predict an appreciable redshift in the light abosprtion properties due to metal-chalcogenide modifications. Thus, we may conclude that the modified surfaces exhibit a redshift in the energy gap, with respect to the unmodified rutile (110) surface. Moreover, modifier-derived states near the Fermi level will have important consequences for the HER activity.

3.3. Photoexcitation model

The energies computed from the photoexcitation model are presented in table 1. First, the model applied to the bare rutile (110) surface yields a vertical energy, E^{vert}, of 2.03 eV. This quantity is equivalent to the optical band gap and indicates that the underestimation of the energy gap, typical of approximate DFT methods, is present in the current computational setup. Nevertheless, this model lends itself to useful qualitative comparisons between the bare surface and the modified systems.

The values for E^{vert} indicate that modification induces a redshift in the energy gap, as was also shown in analysis of the PEDOS plots. Optical gaps of 1.17, 1.11, 1.58 and 1.30 eV are computed for the rutile (110) surface modified with Sn_4S_4, Sn_4Se_4, Zn_4S_4 and Zn_4Se_4, respectively. The excitation energy, E^{exc}, is the energy difference between the singlet ground state and the fully relaxed triplet excited state. Each of the modified surfaces exhibit a reduction in this value, with respect to that computed for the bare rutile (110) surface. The computed relaxation energies, E^{rel}, are larger for the modified systems. E^{rel} represents the energy gained by the system after structural changes and relaxation in the excited state and is a measure of the stability of electron and hole localisation.

To take part in photocatalytic reactions, photoexcited charges must separate and migrate to active surface sites and this entails overcoming the electron–hole binding energy, which is not accounted for in this simple model for photoexcitation. However, low-coordinated surface sites can act as charge traps and suppress carrier recombination [68], and this is captured in our model. Moreover, the computed values E^{rel} are useful as a measure of the stability of charge trapping and indicate that this is enhanced upon modification with the metal chalcogenide nanoclusters. Taken together, the values shown in table 1 indicate that modification of

Table 1. Energies computed from the photoexcitation model. Vertical singlet-triplet energy difference (E^{vert}), the relaxed singlet-triplet energy difference (E^{exc}) and the relaxation energy (E^{relax}) for M_4X_4-modified rutile (110). Values computed for the unmodified TiO_2 rutile (110) surface have been included for reference.

System	E^{vert} (eV)	E^{exc} (eV)	E^{relax} (eV)
Bare r110	2.03	1.60	0.43
Sn_4S_4-r110	1.17	0.16	1.01
Sn_4Se_4-r110	1.11	0.14	0.97
Zn_4S_4-r110	1.58	0.46	1.12
Zn_4Se_4-r110	1.30	0.13	1.17

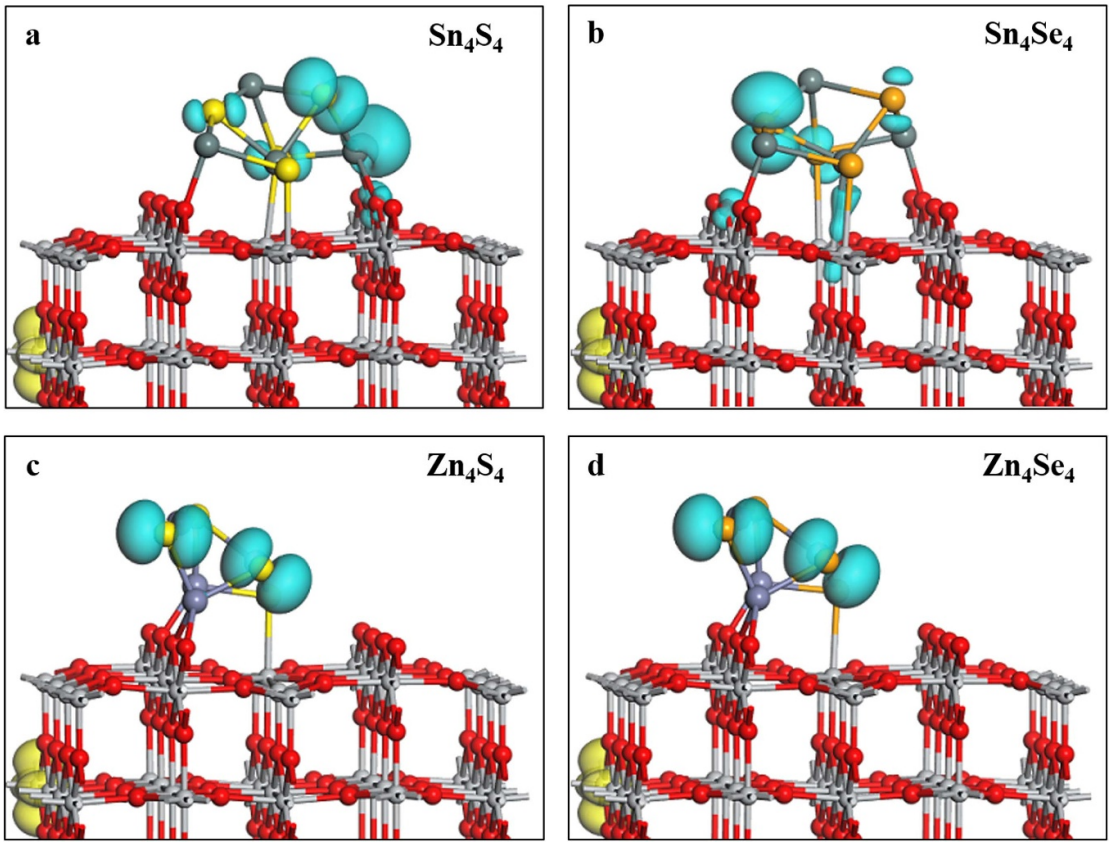

Figure 4. Excess spin density plots computed for the excited state of (a) Sn_4S_4-, (b) Sn_4Se_4-, (c) Zn_4S_4-, and (d) Zn_4Se_4-r110, after structural relaxation. The isosurfaces enclose spin densities of up to 0.02 eV $Å^{-3}$. Electrons are indicated by yellow and holes by blue.

rutile (110) with nanoclusters of composition M_4X_4 induces a redshift in light absorption and enhances the stability of photoexcited charges.

By examining the excess spin density plots, shown in figure 4, in combination with analysis of computed Bader charges and spin magnetisations, we identify at which ions the photoexcited charges localise. For each system, the electrons and holes localise at the surface and modifier, respectively, which promotes charge separation. The yellow isosurfaces show that the electrons localise at sub-surface Ti ions, resulting in a reduction from Ti^{4+} to Ti^{3+}. This is corroborated by an increase in Bader charge from 1.3 electrons for Ti^{4+} to 1.6/1.7 electrons for Ti^{3+} and a computed spin magnetisation of 0.94 μ_B for the reduced Ti^{3+} ion.

For Sn_4S_4-r110, the hole state localises predominantly on an S ion and a neighbouring Sn ion. For the S ion, the Bader charge decreases from 6.9 to 6.7 electrons and this ion has a spin magnetisation of 0.29 μ_B. For the Sn ion, the Bader charge decreases from 12.8 to 12.6 electrons, indicating some hole localisation on Sn, consistent with the DOS analysis; the spin magnetisation for this Sn ion is 0.19 μ_B. For Sn_4Se_4-r110, the hole localises on an Se ion, for which the Bader charge decreases from 6.8 to 6.4 electrons; the spin magnetisation for this ion is 0.41 μ_B.

For both Zn_4S_4-r110 and Zn_4Se_4-r110, the hole state is distributed over two chalcogen ions; the S ions have computed spin magnetisations of 0.27 and 0.39 μ_B, while for the Se ions the spin magnetisations are 0.32 and 0.35 μ_B. For Zn_4S_4-r110, the Bader charges for these S ions decrease from 6.9 and 6.8 electrons to

Table 2. Free energies (in eV) for H adsorption at surface sites (O) and cluster sites (S, Se) of Sn_4S_4-, Sn_4Se_4-, Zn_4S_4-, and Zn_4Se_4-r110. The data presented herein follows from the procedure described in the methodology section and summarized in the schematic in figure 1. For each system and coverage, adsorption at surface sites is more favourable than adsorption at cluster sites. For adsorption of H at cluster sites, adsorption free energies in the active range are highlighted in bold.

System	Site	0H	1H	2H	3H	4H	5H	6H
Sn_4S_4-r110	**O**	0.00	−0.85	−0.36	−0.18	−0.44	−0.16	
	S		−0.34	−0.25	**−0.08**	0.29	**−0.00**	**0.04**
	S + S			**−0.09**	0.35	**0.15**	**−0.13**	0.25
Sn_4Se_4-r110	**O**	0.00	−0.65	−0.59	−0.30	−0.18	−0.12	−0.15
	Se		**−0.12**	0.28	0.28	0.50	0.52	0.51
	Se + Se			0.47				
Zn_4S_4-r110	**O**	0.00	−0.81	−0.32	−0.21	−0.22	−0.06	
	S		−0.35	−0.19	**−0.10**	**−0.08**	**0.02**	**0.12**
	S + S			**0.07**	0.67	**0.12**	0.52	0.74
Zn_4Se_4-r110	**O**	0.00	−0.56	−0.59	−0.25	−0.13	−0.08	
	Se		**0.15**	**0.08**	0.20	0.33	0.40	0.29
	Se + Se			0.45				

6.7 and 6.5 electrons, respectively. Similarly, the Bader charges for the Se ions at which the hole localises in Zn_4Se_4-r110 decrease from 6.8 to 6.5 electrons and from 6.6 to 6.4 electrons. In summary, each of the modified surfaces exhibit a reduction in the optical gap and an enhanced stability of excited charges, with respect to bare rutile (110). Moreover, after modification, the photoexcited electrons and holes are spatially separated; the electrons localise at subsurface Ti sites and the holes localise at chalcogen ions of the supported modifiers.

3.4. Hydrogen adsorption

Next, we examine the free energy of H adsorption at the modified surfaces and, as mentioned in the introduction, we consider that these modified materials will promote HER should they exhibit H adsorption free energies close to thermoneutral, i.e. 0 eV. For practical purposes, values of ΔG_H between −0.15 eV and 0.15 eV are in the active range. For H adsorption at the rutile (110) surface, only the two-fold coordinated O_{br} ions are investigated. After modification, there are five such sites for Sn_4S_4-, Zn_4S_4- and Zn_4Se_4-r110, and six for Sn_4Se_4-r110; full coverage of the surface sites corresponds to five or six H atoms ($N = 5$ or 6). For each surface coverage of $n = (1 \rightarrow N)$H, we identify the most stable configuration for the n^{th} H atom adsorbed at a surface site by computing ΔG_H relative to a surface coverage of $(n-1)$H atoms for each available site, using equation (2). The results of these computations are shown in the rows labelled '**O**' for each surface in table 2.

For surface coverages of between 0 and N hydrogens, we then examine hydrogen adsorption at all chalcogen sites and computed ΔG_H for the most stable chalcogen sites are presented in table 2, in the rows labelled '**X**', (**X** = S, Se). The adsorption free energy of the n^{th} H atom at a cluster site is calculated relative to the surface with $(n-1)$H at surface sites, according to equation (3). Henceforth, we distinguish between 'coverage' and 'surface coverage'; the former refers to the total H coverage, including adsorption sites at the nanoclusters, whereas the latter refers only to H adsorbed on O sites of the rutile (110) support.

For each modified surface, H adsorption at TiO_2 bridging oxygen sites is exothermic for all surface coverages. As the surface coverage increases, approaching full occupation of O_{br} sites, ΔG_H decreases. However, for all coverages, H adsorption at surface sites is more favourable than adsorption at chalcogen sites. Thus, for the n^{th} H atom, ΔG_H for adsorption at a cluster site is computed relative to the system with a surface coverage of $(n-1)$H.

For configurations with a H atom adsorbed at a cluster site with a free energy in the active range, we also investigate ΔG_H for adsorption at a second cluster site. The results of these computations are included in the rows labelled '**X + X**' (**X** = S, Se). All adsorption configurations for the data in table 2 are shown in figure 5, for the example of Sn_4S_4-r110, and for the remaining heterostructures, the adsorption configurations at cluster sites with energies in the active range are summarised in figure 6. All adsorption configurations for the other heterostructures are shown in figures S3–S5 of the supplementary material.

At all coverages, the bonds formed upon H adsorption at anion sites are consistent; O–H, S–H and Se–H bonds measure in the ranges 0.97–1.00 Å, 1.35–1.40 Å and 1.47–1.49 Å, respectively. For the sulphide-modified surfaces, Sn_4S_4-r110 and Zn_4S_4-r110, the first H atoms adsorb strongly at both surface and cluster sites; ΔG_H of −0.85 and −0.81 eV are computed for surface O_{br} sites and the computed ΔG_H is −0.34 and −0.35 eV for S sites. These values are quite exothermic and suggest that, at this coverage, the surface will be hydroxylated and HER is not favourable at the nanocluster as the S–H bond is too stable.

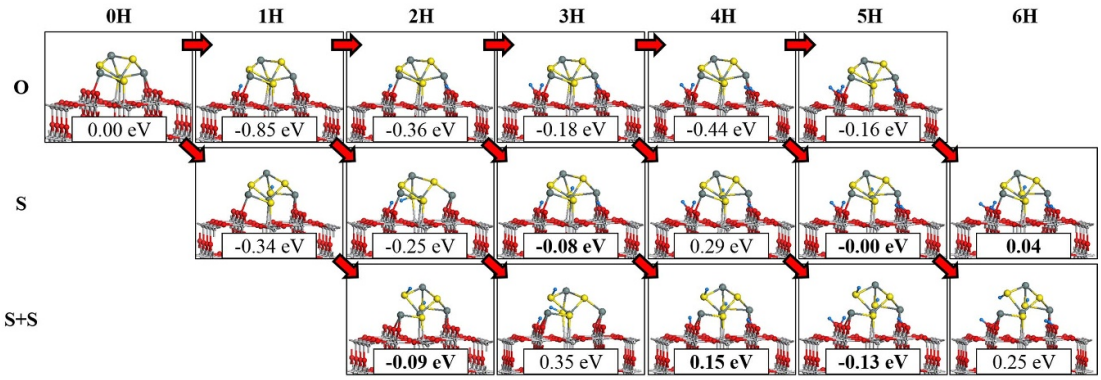

Figure 5. Adsorption configurations of H adsorbed at Sn_4S_4-r110 for coverages between one and six H atoms. The top row shows H adsorbed only at surface (O_{br}) sites, the second row shows configurations in which 1H is adsorbed at a cluster (S) site, at each coverage. The configurations in the third row have 2H adsorbed at S sites, for each coverage. The adsorption free energies, ΔG_H, are included in the insets and the red arrows indicate the configurations relative to which ΔG_H is computed. At all coverages, H adsorption at O_{br} sites is more favourable than adsorption at cluster sites. In this and subsequent figures, values for ΔG_H in the active range are highlighted in bold, for cluster sites.

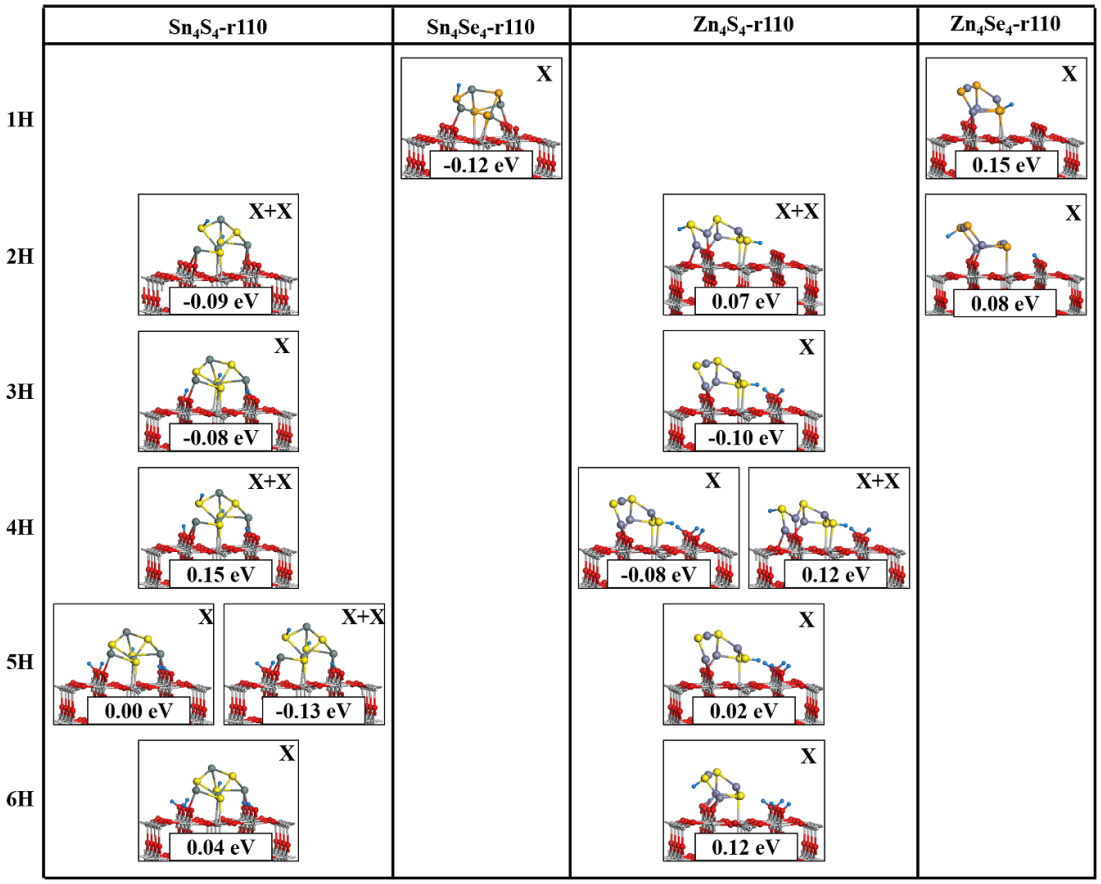

Figure 6. H adsorption configurations with free energies in the range −0.15 eV to +0.15 eV, for adsorption at cluster sites of Sn_4S_4-, Sn_4Se_4-, Zn_4S_4-, and Zn_4Se_4-r110. The total H coverages are shown on the left hand side. 'X' = adsorption of a single H at a chalcogen site of the cluster; 'X + X' = adsorption of two H at chalcogen sites of the cluster.

However, starting from coverages of 2H, the computed ΔG_H for cluster sites are generally in the active range −0.15 eV to 0.15 eV.

By contrast, for Sn_4Se_4-r110, only the first H adsorption free energy at a cluster site is within the active range, irrespective of the surface H coverage. Similarly, for Zn_4Se_4-r110, only two adsorption configurations are in the active range, at coverages of 1H and 2H. For higher coverages, while adsorption at O sites is favourable, adsorption at Se sites is endothermic and the free energies are outside the active range.

In summary, the data presented in table 2 indicate that the sulphide-modified surfaces will be more active in HER, with respect to the selenide-modified surfaces. In general, H adsorption at S sites is more favourable than adsorption at Se sites; adsorption at Se sites is generally highly endothermic. This result is in agreement with a recent study on the stabilisation of hydrogen adsorption on Chevrel-Phase Mo_6X_8 (X = S, Se, Te) electrocatalysts [69]. Through a combination of experiment and computation, the authors reported that H adsorption strength increased with the electronegativity of the chalcogen (S = 2.58; Se = 2.55) [70]. This result manifests in the electronic structure as a lower *p*-band centre. The *p*-band centre is defined as:

$$X_{p-\text{band centre}} = \frac{\int_{-\infty}^{\infty} E \cdot D_{X_p}(E)\,\mathrm{d}E}{\int_{-\infty}^{\infty} D_{X_p}(E)\,\mathrm{d}E} - E_F. \tag{6}$$

This quantity can be extrapolated from the computed PEDOS and values of −2.08, −1.69, −2.23 and −1.97 eV were computed for the chalcogen species of Sn_4S_4-, Sn_4Se_4-, Zn_4S_4- and Zn_4Se_4-r110, respectively. The lower *p*-band centres for the sulphide-modified systems reflect the stronger hydrogen adsorption at cluster sites of these composite surfaces. The computed values for the *p*-band centres are lower for the ZnX modifiers, with respect to the SnX modifiers. However, this does not manifest in appreciable differences in the H adsorption free energies between ZnX and SnX modification, as shown in table 2. Thus, the role of the metal in the M_4X_4 modifiers, whether Sn or Zn, does not appear to affect the HER activity and the nature of the chalcogen, whether S or Se, plays a greater role. Finally, hydroxylation of the rutile support, beyond a surface coverage of 1H, does not qualitatively affect the strength of adsorption of H at cluster sites.

For each of the H adsorption configurations at cluster sites with ΔG_H in the range −0.15 eV to 0.15 eV, highlighted in bold in table 2, we examine the subsequent Heyrovsky step in which an H atom interactions with H bound at S or Se of the nanocluster. This results in the formation and desorption of a H_2 molecule in a process which amounts to the reverse of H adsorption; thus, the free energy corrections, $\Delta E_{ZPE} - T\Delta S_H$, are the negative of those computed for H adsorption, i.e. −0.29 eV and −0.26 eV for desorption from S and Se, respectively. For Sn_4S_4-r110, of the six adsorption configurations with ΔG_H in the active range, the desorption free energies are in the range −0.20 eV to +0.22 eV. For the four active configurations on Zn_4S_4-r110, the desorption energies are in the range −0.34 eV to 0.14 eV. The free energies are 0.40 eV for desorption from Sn_4Se_4-r110 and −0.19 and 0.53 eV for desorption from Zn_4Se_4-r110. This suggests that formation of H_2 through the Heyrovsky step should be favourable on metal sulphide modified TiO_2.

4. Conclusions

Metal chalcogenides have emerged as promising candidates for HER catalysis. Extensive experimental and computational studies of TMDs have revealed that low-coordinated chalcogen sites are active sites for HER. This is attributed to the near optimal adsorption free energy of H at chalcogen sites.

In this work, we have examined, via DFT + U computations, the surface modification of TiO_2 rutile (110) with nanoclusters of composition M_4X_4 (M = Sn, Zn; X = S, Se). Surface modification strategies aim to combine the desirable properties of the substrate (TiO_2) with those of the nanocluster modifiers. In this instance, the M_4X_4 modifiers provide low-coordinated chalcogen sites, which we have investigated for their HER activity via computations of the free energy of H adsorption.

Our results indicate that the M_4X_4 modifiers bind to the rutile surface with the formation of interfacial M–O and Ti–X bonds. The modification induces a red shift in light absorption due to the emergence of occupied, nanocluster-derived (predominantly chalcogen 2*p*) states in the titania energy gap. In addition, modification with M_4X_4 nanoclusters promotes the spatial separation of photoexcited charges and enhances their stability in the excited state.

Analysis of the free energies of H adsorption, ΔG_H, reveals that the sulphide modifiers exhibit values close to thermoneutral, (−0.15 eV, +0.15 eV), for most H coverages, whereas this is only true for the selenide modifiers at low coverages. This is a widely accepted descriptor for HER activity and suggests that sulphide-modification will promote the HER to a greater extent than selenide modification. In general, H binding at sulphur sites is more favourable than at selenium sites; we attribute this to the higher electronegativity of S, with respect to Se. This effect is manifested in the computed *p*-band centres of the modified systems—the sulphide-modified systems exhibit lower *p*-band centres than the selenide-modified systems.

In conclusion, modification of titania with dispersed metal chalcogenide nanoclusters has the potential to enhance the HER activity of the titania support. However, despite their desirable photocatalytic properties, chalcogenides can suffer from poor chemical stability [71] and this must be accounted for in the design of practical photocatalysts. While metal chalcogenides can oxidise in aqueous environments, many of the

chalcogenide catalysts presented in our recent review of non-metal oxide catalysts for HER exhibit stable performance under HER conditions [8]. Thus, one strategy for preserving the integrity of metal chalcogenide catalysts for water splitting applications will entail the design of a suitable photoelectrochemical cell, in which the OER and HER proceed in separate compartments. Another approach to promote the stability is to deposit very thin, protective layers via ALD or similar techniques [72–74].

Careful analysis is required to elucidate the impact of modification on the properties which govern the photocatalytic HER activity. However, rational selection of the composition of the modifiers, in combination with first principles computations of appropriate material descriptors can facilitate high-throughput screening of candidate materials.

Acknowledgments

We acknowledge support from Science Foundation Ireland through the US-Ireland R&D Partnership Programme, Grant No. SFI/US/14/E2915 and the ERA.Net for Materials Research and Innovation (M-ERA.Net 2), Horizon 2020 Grant Agreement No. 685451, SFI Grant No. SFI/16/M-ERA/3418 (RATOCAT). We acknowledge access to SFI funded computing resources at Tyndall Institute and the SFI/HEA funded Irish Centre for High End Computing. We are grateful for support from the COST Action CM1104 'Reducible Metal Oxides, Structure and Function'

ORCID iDs

Stephen Rhatigan https://orcid.org/0000-0002-9652-468X
Michael Nolan https://orcid.org/0000-0002-5224-8580

References

[1] Fujishima A, Zhang X and Tryk D A 2008 TiO_2 photocatalysis and related surface phenomena *Surf. Sci. Rep.* **63** 515–82
[2] Ni M, Leung M K H, Leung D Y C and Sumathy K 2007 A review and recent developments in photocatalytic water-splitting using TiO_2 for hydrogen production *Renew. Sustain. Energy Rev.* **11** 401–25
[3] Dimitrijevic N M, Vijayan B K, Poluektov O G, Rajh T, Gray K A, He H and Zapol P 2011 Role of water and carbonates in photocatalytic transformation of CO_2 to CH_4 on Titania *J. Am. Chem. Soc.* **133** 3964–71
[4] Habisreutinger S N, Schmidt-Mende L and Stolarczyk J K 2013 Photocatalytic reduction of CO_2 on TiO_2 and other semiconductors *Angew. Chem., Int. Ed.* **52** 7372–408
[5] Pelaez M *et al* 2012 A review on the visible light active titanium dioxide photocatalysts for environmental applications *Appl. Catal.* B **125** 331–49
[6] Etacheri V, Di Valentin C, Schneider J, Bahnemann D and Pillai S C 2015 Visible-light activation of TiO_2 photocatalysts: advances in theory and experiments *J. Photochem. Photobiol.* C **25** 1–29
[7] Tada H, Jin Q, Iwaszuk A and Nolan M 2014 Molecular-scale transition metal oxide nanocluster surface-modified titanium dioxide as solar-activated environmental catalysts *J. Phys. Chem.* C **118** 12077–86
[8] Rhatigan S, Michel M C and Nolan M 2020 Hydrogen evolution on non-metal oxide catalysts *J. Phys. Energy* **2** 042002
[9] Huang Z-F, Wang J, Peng Y, Jung C-Y, Fisher A and Wang X 2017 Design of efficient bifunctional oxygen reduction/evolution electrocatalyst: recent advances and perspectives *Adv. Energy Mater.* **7** 1700544
[10] Zou X and Zhang Y 2015 Noble metal-free hydrogen evolution catalysts for water splitting *Chem. Soc. Rev.* **44** 5148–80
[11] Huang X, Zeng Z and Zhang H 2013 Metal dichalcogenide nanosheets: preparation, properties and applications *Chem. Soc. Rev.* **42** 1934–46
[12] McAllister J, Bandeira N A G, McGlynn J C, Ganin A Y, Song Y-F, Bo C and Miras H N 2019 Tuning and mechanistic insights of metal chalcogenide molecular catalysts for the hydrogen-evolution reaction *Nat. Commun.* **10** 370
[13] Bollinger M V, Jacobsen K W and Nørskov J K 2003 Atomic and electronic structure of MoS_2 nanoparticles *Phys. Rev.* B **67** 085410
[14] Lauritsen J V, Bollinger M V, Lægsgaard E, Jacobsen K W, Nørskov J K, Clausen B S, Topsøe H and Besenbacher F 2004 Atomic-scale insight into structure and morphology changes of MoS_2 nanoclusters in hydrotreating catalysts *J. Catal.* **221** 510–22
[15] Jaramillo T F, Jørgensen K P, Bonde J, Nielsen J H, Horch S and Chorkendorff I 2007 Identification of active edge sites for electrochemical H_2 evolution from MoS_2 nanocatalysts *Science* **317** 100–2
[16] Xiao P, Chen W and Wang X 2015 A review of phosphide-based materials for electrocatalytic hydrogen evolution *Adv. Energy Mater.* **5** 1500985
[17] Hu C, Zhang L and Gong J 2019 Recent progress made in the mechanism comprehension and design of electrocatalysts for alkaline water splitting *Energy Environ. Sci.* **12** 2620–45
[18] Vesborg P C K, Seger B and Chorkendorff I 2015 Recent development in hydrogen evolution reaction catalysts and their practical implementation *J. Phys. Chem. Lett.* **6** 951–7
[19] Dubouis N and Grimaud A 2019 The hydrogen evolution reaction: from material to interfacial descriptors *Chem. Sci.* **10** 9165–81
[20] Hinnemann B, Moses P G, Bonde J, Jørgensen K P, Nielsen J H, Horch S, Chorkendorff I and Nørskov J K 2005 Biomimetic hydrogen evolution: MoS_2 nanoparticles as catalyst for hydrogen evolution *J. Am. Chem. Soc.* **127** 5308–9
[21] Bonde J, Moses P G, Jaramillo T F, Nørskov J K and Chorkendorff I 2009 Hydrogen evolution on nano-particulate transition metal sulfides *Faraday Discuss.* **140** 219–31
[22] Tsai C, Chan K, Abild-Pedersen F and Nørskov J K 2014 Active edge sites in $MoSe_2$ and WSe_2 catalysts for the hydrogen evolution reaction: a density functional study *Phys. Chem. Chem. Phys.* **16** 13156–64
[23] Tsai C, Chan K, Nørskov J K and Abild-Pedersen F 2015 Theoretical insights into the hydrogen evolution activity of layered transition metal dichalcogenides *Surf. Sci.* **640** 133–40

[24] Gajaria T K, Roondhe B, Dabhi S D, Śpiewak P, Kurzydłowski K J and Jha P K 2020 Hydrogen evolution reaction electrocatalysis trends of confined gallium phosphide with substitutional defects *Int. J. Hydrog. Energy* **45** 23928–36

[25] Gao Y, Li H, Wang J, Ma J and Ren H 2019 New insight on hydrogen evolution reaction activity of MoP_2 from theoretical perspective *Nanomaterials* **9** 1270

[26] Liang Z, Zhong X, Li T, Chen M and Feng G 2019 DFT study on the hydrogen evolution reaction for different facets of Co_2P *ChemElectroChem* **6** 260–7

[27] Libera J A, Elam J W, Sather N F, Rajh T and Dimitrijevic N M 2010 Iron(III)-oxo centers on TiO_2 for visible-light photocatalysis *Chem. Mater.* **22** 409–13

[28] Majrik K, Pászti Z, Korecz L, Trif L, Domján A, Bonura G, Cannilla C, Frusteri F, Tompos A and Tálas E 2018 Study of PtO_x/TiO_2 photocatalysts in the photocatalytic reforming of glycerol: the role of co-catalyst formation *Materials* **11** 1927

[29] Munnik P, De Jongh P E and De Jong K P 2015 Recent developments in the synthesis of supported catalysts *Chem. Rev.* **115** 6687–718

[30] Lamai W, Bunphung A, Junumpun I and Wongkaew A 2019 Synthesis and characterization of Ni@Pt core-shell catalyst over TiO_2 support prepared by incipient wetness impregnation and electroless deposition *Mater. Today* **17** 1396–402

[31] Jin Q, Fujishima M and Tada H 2011 Visible-light-active iron oxide-modified anatase titanium(IV) dioxide *J. Phys. Chem.* C **115** 6478–83

[32] Rhatigan S, Sokalu E, Nolan M and Colón G 2020 Surface modification of rutile TiO_2 with alkaline-earth oxide nanoclusters for enhanced oxygen evolution *ACS Appl. Nano Mater.* **3** 6017–33

[33] Rhatigan S and Nolan M 2018 CO_2 and water activation on ceria nanocluster modified TiO_2 rutile (110) *J. Mater. Chem.* A **6** 9139–52

[34] Fronzi M, Daly W and Nolan M 2016 Reactivity of metal oxide nanocluster modified rutile and anatase TiO_2: oxygen vacancy formation and CO_2 interaction *Appl. Catal.* A **521** 240–9

[35] Tamura H, Mita K, Tanaka A and Ito M 2001 Mechanism of hydroxylation of metal oxide surfaces *J. Colloid Interface Sci.* **243** 202–7

[36] Kresse G and Hafner J 1994 *Ab initio* molecular-dynamics simulation of the liquid-metal-amorphous-semiconductor transition in germanium *Phys. Rev.* B **49** 14251–69

[37] Furthmüller J, Hafner J and Kresse G 1996 Dimer reconstruction and electronic surface states on clean and hydrogenated diamond (100) surfaces *Phys. Rev.* B **53** 7334–51

[38] Blöchl P E 1994 Projector augmented-wave method *Phys. Rev.* B **50** 17953–79

[39] Kresse G and Joubert D 1999 From ultrasoft pseudopotentials to the projector augmented-wave method *Phys. Rev.* B **59** 1758–75

[40] Perdew J P, Burke K and Ernzerhof M 1996 Generalized gradient approximation made simple *Phys. Rev. Lett.* **77** 3865–8

[41] Rhatigan S and Nolan M 2019 Activation of water on MnO_x-nanocluster-modified rutile (110) and Anatase (101) TiO_2 and the role of cation reduction *Front. Chem.* **7**

[42] Rhatigan S and Nolan M 2018 Impact of surface hydroxylation in MgO-/SnO-nanocluster modified TiO_2 anatase (101) composites on visible light absorption, charge separation and reducibility *Chin. Chem. Lett.* **29** 757–64

[43] Kumaravel V *et al* 2019 Indium-doped TiO_2 photocatalysts with high-temperature anatase stability *J. Phys. Chem.* C **123** 21083–96

[44] Kumaravel V *et al* 2020 Mo doped TiO_2: impact on oxygen vacancies, anatase phase stability and photocatalytic activity *J. Phys. Mater.* **3** 025008

[45] Koch W and Holthausen M C 2001 The quest for approximate exchange-correlation functionals *A Chemist's Guide to Density Functional Theory* (New York: Wiley) pp 65–91

[46] Adamo C and Barone V 1999 Toward reliable density functional methods without adjustable parameters: the PBE0 model *J. Chem. Phys.* **110** 6158–70

[47] Morgan B J and Watson G W 2007 A DFT + U description of oxygen vacancies at the TiO_2 rutile (110) surface *Surf. Sci.* **601** 5034–41

[48] Nolan M, Elliott S D, Mulley J S, Bennett R A, Basham M and Mulheran P 2008 Electronic structure of point defects in controlled self-doping of the TiO_2 (110) surface: combined photoemission spectroscopy and density functional theory study *Phys. Rev.* B **77** 235424

[49] Iwaszuk A and Nolan M 2011 Reactivity of sub 1 nm supported clusters: $(TiO_2)_n$ clusters supported on rutile TiO_2 (110) *Phys. Chem. Chem. Phys.* **13** 4963–73

[50] Nolan M 2011 Electronic coupling in iron oxide-modified TiO_2 leads to a reduced band gap and charge separation for visible light active photocatalysis *Phys. Chem. Chem. Phys.* **13** 18194–9

[51] Fronzi M, Iwaszuk A, Lucid A and Nolan M 2016 Metal oxide nanocluster-modified TiO_2 as solar activated photocatalyst materials *J. Phys.: Condens. Matter* **28** 074006

[52] Fronzi M and Nolan M 2017 Surface modification of perfect and hydroxylated TiO_2 rutile (110) and anatase (101) with chromium oxide nanoclusters *ACS Omega* **2** 6795–808

[53] Iwaszuk A, Lucid A K, Razeeb K M and Nolan M 2014 First principles investigation of anion-controlled red shift in light absorption in ZnX (X = O, S, Se) nanocluster modified rutile TiO_2 *J. Mater. Chem.* A **2** 18796–805

[54] Anisimov V I, Zaanen J and Andersen O K 1991 Band theory and Mott insulators: Hubbard *U* instead of Stoner *I Phys. Rev.* B **44** 943–54

[55] Dudarev S L, Botton G A, Savrasov S Y, Humphreys C J and Sutton A P 1998 Electron-energy-loss spectra and the structural stability of nickel oxide: an LSDA + U study *Phys. Rev.* B **57** 1505–9

[56] Byrne C, Rhatigan S, Hermosilla D, Merayo N, Blanco Á, Michel M C, Hinder S, Nolan M and Pillai S 2019 Modification of TiO_2 with hBN: high temperature anatase phase stabilisation and photocatalytic degradation of 1,4-dioxane *J. Phys. Mater.* **3** 015009

[57] Nolan M, Iwaszuk A and Tada H 2012 Molecular metal oxide cluster-surface modified titanium dioxide photocatalysts *Aust. J. Chem.* **65** 624–32

[58] Iwaszuk A, Nolan M, Jin Q, Fujishima M and Tada H 2013 Origin of the visible-light response of nickel(II) oxide cluster surface modified titanium(IV) dioxide *J. Phys. Chem.* C **117** 2709–18

[59] Jin Q, Fujishima M, Nolan M, Iwaszuk A and Tada H 2012 Photocatalytic activities of tin(IV) oxide surface-modified titanium(IV) dioxide show a strong sensitivity to the TiO_2 crystal form *J. Phys. Chem.* C **116** 12621–6

[60] Yadav P S and Pandey D K 2012 A DFT study for the structural and electronic properties of Zn_mSe_n nanoclusters *Appl. Nanosci.* **2** 351–7

[61] Sharma M, Mishra D and Kumar J 2019 First-principles study of the structural and electronic properties of bulk ZnS and small Zn_nS_n nanoclusters in the framework of the DFT + U method *Phys. Rev.* B **100** 045151

[62] Liao P, Keith J A and Carter E A 2012 Water oxidation on pure and doped hematite (0001) surfaces: prediction of Co and Ni as effective dopants for electrocatalysis *J. Am. Chem. Soc.* **134** 13296–309
[63] Baraiya B A, Mankad V and Jha P K 2018 Adsorption energetics of atoms and diatomic gases with electrocatalysis approach towards hydrogen and oxygen evolution reaction on Pt surfaces *ChemistrySelect* **3** 10515–25
[64] Nørskov J K, Bligaard T, Logadottir A, Kitchin J R, Chen J G, Pandelov S and Stimming U 2005 Trends in the exchange current for hydrogen evolution *J. Electrochem. Soc.* **152** J23–6
[65] Shannon R 1976 Revised effective ionic radii and systematic studies of interatomic distances in halides and chalcogenides *Acta Crystallogr.* A **32** 751–67
[66] Walsh A and Watson G W 2005 Influence of the anion on lone pair formation in Sn(II) monochalcogenides: a DFT study *J. Phys. Chem.* B **109** 18868–75
[67] Iwaszuk A and Nolan M 2013 SnO-nanocluster modified anatase TiO_2 photocatalyst: exploiting the Sn(II) lone pair for a new photocatalyst material with visible light absorption and charge carrier separation *J. Mater. Chem.* A **1** 6670–7
[68] Kang Q, Cao J, Zhang Y, Liu L, Xu H and Ye J 2013 Reduced TiO_2 nanotube arrays for photoelectrochemical water splitting *J. Mater. Chem.* A **1** 5766–74
[69] Ortiz-Rodríguez J C, Singstock N R, Perryman J T, Hyler F P, Jones S J, Holder A M, Musgrave C B and Velázquez J M 2020 Stabilizing hydrogen adsorption through theory-guided chalcogen substitution in Chevrel-phase Mo_6X_8 (X = S, Se, Te) electrocatalysts *ACS Appl. Mater. Interfaces* **12** 35995–6003
[70] Allred A L 1961 Electronegativity values from thermochemical data *J. Inorg. Nucl. Chem.* **17** 215–21
[71] Nie L and Zhang Q 2017 Recent progress in crystalline metal chalcogenides as efficient photocatalysts for organic pollutant degradation *Inorg. Chem. Front.* **4** 1953–62
[72] Dasgupta N P, Lee H-B-R, Bent S F and Weiss P S 2016 Recent advances in atomic layer deposition *Chem. Mater.* **28** 1943–7
[73] Noh J H, Lee S, Kim J Y, Lee J-K, Han H S, Cho C M, Cho I S, Jung H S and Hong K S 2009 Functional multilayered transparent conducting oxide thin films for photovoltaic devices *J. Phys. Chem.* C **113** 1083–7
[74] Yang W, Prabhakar R R, Tan J, Tilley S D and Moon J 2019 Strategies for enhancing the photocurrent, photovoltage, and stability of photoelectrodes for photoelectrochemical water splitting *Chem. Soc. Rev.* **48** 4979–5015